M.Sc.: Ecological and Environmental Engineering
Department of Environment
University of the Aegean

# Title: Study of downward longwave radiation on the decadal scale. Investigation of multifractal characteristics and long-term memory

Stathopoulos Vassilios
Under the supervision of: Matsoukas Christos

30/10/2012

# Contents

**Abstract**

We study the time fluctuations of Downward Longwave Radiation (DLR) using Multi-Fractal Detrended Fluctuation Analysis (MF-DFA) in decadal scale. In most stations non-stationary signal is observed for micro-scales, comparable to those of meteorological processes. DLR presents power law scaling for time scales of about ten days to five years. These different scaling regions are delimited from the emergence of a crossover that marks the transition to a positively correlated signal referred to as long-memory. In several stations presenting the common feature of strong maritime influence, fluctuation function follows 1/f noise in micro-scales. These stations' fluctuations are most likely affected by oscillatory trends. This is revealed by examining second order fluctuation function $F_2(s)$ and further confirmation is derived from multifractal analysis where scaling exponents spectrum is corrupted in a typical way, characteristic of periodicities presence. In west Pacific equatorial stations periodicity seems to be ENSO, though this cannot be clearly considered a fact. In stations where no obvious oscillatory trend is observed for $F_2(s)$, mean memory is 0.63. Dependence of fluctuations scaling exponents on the order q approaches the therotical behavior for Gaussian data. Deviations possibly occur due to short range correlations embedded in the data.

# Chapter 1

# Introduction

In the ongoing discussion for climate change it is important to recognize the elements that dictate the variability of physical quantities. Downward Longwave Radiation (DLR) constitutes a climate quantity, that is characteristic of the processes present in the planet. The time evolution of its fluctuations is related to the internal variability of the system but it can also have anthropogenic origin. Long-term memory reffers to power law scaling of the fluctuations in meso and large time scales and has been observed in several physical records such as temperature[1, 2], stream flows[3, 4] and prehipitation[5, 3, 4]. The study of the observed fluctuations in a decadal scale is a useful tool for evaluating the predictions about DLR made by models. If predictions violate the observed correlation properties of the fluctuations their reliability is questioned. Climate models construction is based on computational methods in order to simulate the processes occurring in the planet and arising from the interactions among atmosphere, oceans, glaciers, and Earth's surface, finally resulting in shaping the climate. Considering that the calculated radiation involves a diversity of climatic parameters, possible agreement between observations and models predictions acts as an indirect verification of many natural processes [6, 7, 8, 9, 10, 11]. For this reason, in the present study, the analysis of time fluctuations of DLR will be attempted, intending the investigation of climate 'memory' and multifractal characteristics, e.g. the existence of long-range statistical correlations, using Multi-Fractal Detrended Fluctuation Analysis (MF-DFA) [12].

# Chapter 2

# Background

## 2.1 Multi-Fractal Detrended Fluctuation Analysis (MF-DFA)

Detrended Fluctuation Analysis (DFA) is a technique for analyzing data, that was first proposed by Peng et al. [13] and has been used in a variety of fields, for the investigation of temporal correlations of data. The advantage of DFA compared to other methods of characterizing correlation properties, such as Spectral Analysis, is that it holds for non-stationary timeseries [5, 1] while its computational implementation is comparatively simple, even for large data sets. Kantelhardt et al. [12] introduced a generalized version of DFA, the multifractal DFA (MF-DFA) that will be described subsequently.

The method consists of five successive steps.

1. For a compact support, i.e. no zero values included, timeseries of length $N$, $u(i)(i = 1 \dots N)$, its mean $\bar{u}$ is subtracted, creating a timeseries of anomalies. The profile $y(i)$ is determined as the cumulative sum of these anomalies:

$$y(i) = \sum_{i=1}^{N} [u(i) - \bar{u}] \tag{2.1}$$

   Note that in order to avoid spurious results, it is desirable that the timeseries $u(i)$ be deseasonalized [4].

2. The timeseries is divided into $N_s \equiv int(N/s)$ non-overlapping segments of length $s$. In order to include all data points which maybe were excluded because $mod(N/s) \neq 0$, the same procedure is followed starting from the end of the timeseries and proceeding towards the start, thus giving a total of $2N_s$ segments. A curve corresponding to $l$-order polynomial is fitted to each segment $n$ and the variance of the residuals between $y$ and its $l$-order fit $y_n(i), i = 1, \dots, s$ is determined:

$$F^2(n, s) = \frac{1}{s} \sum_{i=1}^{s} \{y[(n-1)s + i] - y_n(i)\}^2 \tag{2.2}$$

   for the first $n = 1, \dots, N_s$ segments, while for the $n = N_s + 1, \dots, 2N_s$ segments:

$$F^2(n, s) = \frac{1}{s} \sum_{i=1}^{s} \{y[N - (n - N_s)s + i] - y_n(i)\}^2 \tag{2.3}$$

   The order $l = 1, 2, \dots$ of the polynomial used for detrending, eliminates possible trends of order $l - 1$ in the timeseries [14] and the indicator for $l$-order DFA is DFA$l$. Up to this step MF-DFA is exactly the same as common DFA.

3. The mean of all equal-length segments is calculated, resulting in the $q$th order fluctuation function:

$$F_q(s) = \Big\{ \frac{1}{2N_s} \sum_{n=1}^{2N_s} [F^2(n,s)]^{q/2} \Big\}^{1/q} \tag{2.4}$$

The value of $q$ can be any real number, but for $q = 0$ the exponent is diverging, and a different averaging method has to be used [12]. If $q = 0$, logarithmic averaging is needed:

$$F_0(s) \equiv \exp\Big( \frac{1}{4N_s} \sum_{n=1}^{2N_s} \ln[F^2(n,s)] \Big) \tag{2.5}$$

4. This procedure is done for segments $s$ up to $N/4$, since the mean $F_q$ for larger segments is estimated from a very small sample size, and the results become evidently uncertain [12]. Common DFA is a subcase of MF-DFA for $q = 2$.

5. Finally, $F_q(s)$ versus $s$ are plotted on a log-log scale and the existence of scaling is examined for small and large scales. If the fluctuation function is described by:

$$F_q(s) \sim s^{h(q)} \tag{2.6}$$

then scaling is established, meaning that there is no characteristic time scale for the autocorrelation of the timeseries. The scaling exponent $h(q)$ is calculated as the slope of the line fitted to the log-log plot for different values of $q$.

The value of *h(2)* defines the type of the self-correlation of the timeseries. If:

- $0 < h(2) < 0.5$, then an anti-correlation exists, i.e. small values of the time series tend to be followed by large values, and vice versa.
- $h(2) \approx 0.5$, indicates no correlation is present, i.e. the timeseries is white noise.
- $0.5 < h(2) < 1$, a positive correlation is established, i.e. small values of the times series tend to be followed by small values, while large values tend to be followed by large values.
- $h(2) \approx 1$, $1/f$ noise (flicker or pink noise) is detected.
- $h(2) > 1$, non-stationary signal.
- $h(2) \approx 1.5$, random walk noise (red, Brownian, or brown noise).

If $h(q)$ displays constancy within a certain range of $q$ values, then the timeseries is characterized as monofractal, else multifractality is assumed and further analysis has to be conducted.

From equation 2.4 one can observe that when $q$ is negative, small fluctuations prevail in the sum $F^2(n,s)$ and $F_q(s)$ refers to how small fluctuations scale [12]. On the contrary, for positive $q$ values, the sum $F^2(n,s)$ is dominated by large fluctuations, so $F_q(s)$ describes how large fluctuations scale.

For large segments the fluctuation function $F_q(s)$ is less dependent on $q$. This can be made clearer considering that for $s = N$, $N_s = 1$ and the sum in Eq. 2.4 is calculated for two identical segments, and $q$ is canceled off. At this extreme, $F_q(s)$ is totally independent of $q$. Moreover, for $s \ll N$, if $q < 0$ the fluctuation function $F_q(s)$ is dominated by small fluctuations and takes smaller values than $F_q(s)$ for large $q$. Summarizing, $F_q(s \ll N)$ for small $q$ tends to be smaller than $F_q(s \ll N)$ for large $q$. At the same time $F_q(s \approx N)$ is roughly the same for small and large $q$. Therefore, the slope of the $F_q(s)$ with $s$, i.e. the scaling exponent $h(q)$ decreases with increasing $q$ [12].

## 2.2 Effects of non-stationarity and trends

Non-stationarity of real data can involve missing values, outliers, trends, and mixed properties of the data. Trends can be linear, periodic, or power-law. Application of MF-DFA on synthetic data, with known properties, can provide the comparative background for interpreting the results derived from real data. Such studies on synthetic data were performed by Chen et al. [15]. First, they generated a synthetic data set (also referred to as noise), with prescribed long-term memory characteristics. Then, linear, periodic, and power-law trends were superimposed on the noise. The analysis by means of DFA showed that a superposition rule can be applied to obtain the fluctuation function:

$$F_{nt}^2 = F_n^2 + F_t^2 \tag{2.7}$$

where $F_n$, $F_t$, and $F_{nt}$ are the fluctuation functions of the noise, trend, and noise with superimposed trend, respectively.

Linear trends are recognized and their effect can be easily eliminated. They produce a crossover at a scale that is defined from the competition of $F_t$ and $F_n$. Before the crossover, the noise dominates and $F_{nt} \approx F_n$, while after the crossover $F_{nt} \approx F_t$. Orders of DFA higher than the order of the trend, eliminate the crossover (perfect fit at the detrending procedure of Eq. 2.3) and $F_{nt}$ scales like $F_n$.

Sinusoidal trends split $F_{nt}$ in four regimes by inducing three crossovers (Fig. 2.1). The behavior of $F_{nt}$ is again decided by the competition of $F_n$ and $F_t$. The noise prevails over the trend for $s$ values much smaller than the trend period, because the sinusoidal trend on this scale can be approximated by linear segments, which are easily detrended by DFA. For larger $s$, the sinusoidal signal cannot be detrended and the first crossover appears. After this crossover $F_{nt} \approx F_t$. At this region scaling of $F_t$ can be approximated by a linear trend scaling with adjusted parameters. Sinusoidal fluctuations are limited by the sine amplitude ($A_s$). So a second crossover, at a scale proportional to the period of the trend, occurs when maximum is reached for $F_t$. Right before the second crossover starts a transitional behavior with quadratic shape. This behavior ends with the emergence of a third crossover where $F_n$ prevails again.

Chen et al. [16] explored how correlated and anti-correlated data are affected by several types of non-stationarity, such as incomplete records with stitched segments or records with added spikes and applied a superposition rule again (Eq. 2.7). For positively correlated data with incomplete records up to 50% DFA results are little or not affected. On the contrary, implementation of DFA on anti-correlated data with this sort of non-stationarity introduces a crossover which divides scaling into two regions, an anti-correlated one before the crossover, followed by uncorrelated behavior after the crossover. Outliers induce a crossover at small scales. For correlated data, this crossover marks a switch from uncorrelated to correlated behavior, similar to the original stationary signal. For anti-correlated data, a crossover also appears at small scales. It splits scaling into an anti-correlated and a white noise regime. Scaling exponent of the initial signal is similar to the one before the crossover. They also reported that mixing certain size segments with different local properties, e.g. standard deviations or correlations

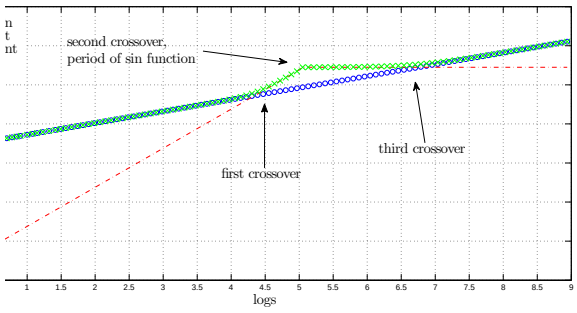


Figure 2.1: Superposition fluctuation function ($F_{nt}$) of sinusoidal trend ($F_t$) and correlated noise ($F_n$)

exponents, produces a result that is related in a specific way to the segments size as well as their mixing ratio.

Ludescher et al. [17] applied MF-DFA to test how long-term correlated and multifractal data records are affected by the presence of additive white noise, short-term autocorrelated noise, and periodic trends.

Adding white noise to monofractal correlated data does not result in a spurious multifractality for several noise amplitudes. However, the observed scaling exponent is affected if the amplitude of the white noise increases. Multifractality of data is corrupted by imposed white noise. Initially the moments for $q < 0$ are highly underestimated, while at a sufficiently large noise amplitude the multifractality vanishes and the signal behaves as white noise. Next, the addition of short-memory noise described by a first order autoregression (AR1) equation is considered. For monofractal data AR1 generates a crossover at a scale comparable to the decay time of the autocorrelation function. The position of the crossover increases with decreasing $q$. So correct scaling exponents can be observed for high $q$ values, because the exponents are estimated at the large $s$ end, which is less probably affected by the crossover for large $q$. Adding short AR1 memory to multifractal data results in decreasing multifractality range with the amplitude of the AR1 process (Fig. 2.2). Finally, investigation of how multifractality is affected by seasonal trends, reaches the reasonable conclusion that if crossovers due to the seasonal trend appear in the large $s$ regime, scaling exponents are affected and so does the pattern of multifractal scaling. The position of the crossovers is comparable to the period of the seasonality as well as on the seasonal trend amplitude.

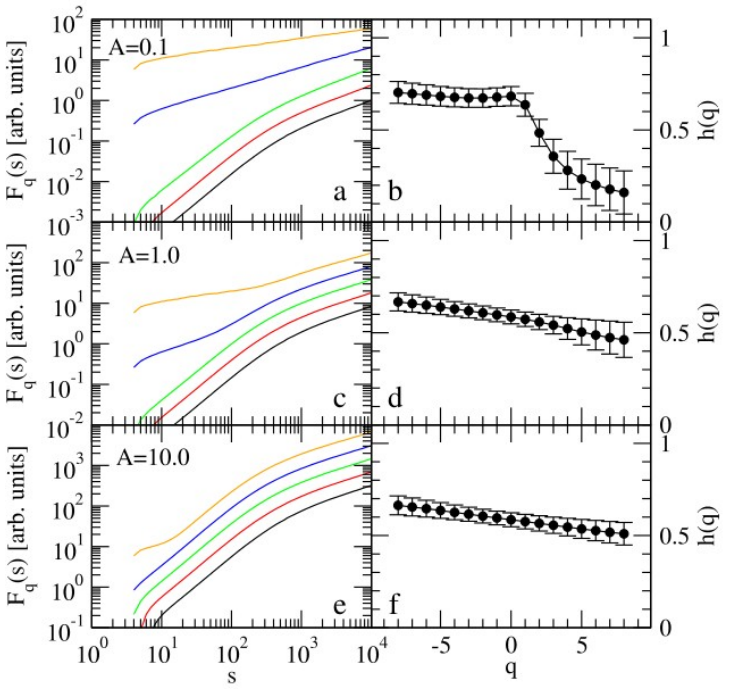


Figure 2.2: Corrupted multifractality and crossover generation from superposed AR1 process with increasing amplitude ($A$)(figure from [17])

## 2.3 Limitations and drawbacks

In order to check if multifractal scaling is due to a broad probability density function or a result of long-range correlations (Noah phenomenon versus Joseph phenomenon) shuffling the data is necessary [12]. Shuffling destroys all possible correlations, so for $q = 2$ a scaling exponent $\sim 0.5$ corresponding to uncorrelated behavior should be observed. If so, scaling can be attributed to long-range correlations and memory existence can be established. There are some limitations to the implementation of MF-DFA regarding long 'memory', though. These limitations involve how the finite size of the timeseries affects the conjecture of long memory existence, raising questions e.g. can the observed scaling exponent be considered a manifestation of true long-range correlation and not a product of an AR process [18]? The findings of MF-DFA have to be carefully interpreted, with respect to the size of the timeseries compared to the scales of the natural processes involved, as well as to the data resolution.

Simoniello et al. [19] and Lanfredi et al. [20] draw the conclusion that scaling establishment through a simple straight line fit in a log-log plot is insufficient due to the nature of the logarithm. Examining local slopes systematic deviations from constant behavior raises questions about power-law functional reliability. This can be regarded as DFA being sensitive but not specific in detecting power-law scaling as proposed by Maraun et al. [18]. A demonstration of this claim was made by Lanfredi et al. [20], where a bivariate Markov model was found to cause long-term correlations in a temperature timeseries, including scale invariance.

Lovejoy et al. [21] argue in a discussion about different multifractal approaches, that MF-DFA is capable of estimating scaling exponents for $q = 2$ but question the ability of MF-DFA and other methods to detect multifractal behavior.

## 2.4 Application on geophysical records

Weber et al. in 2001 [22] refuted the claim of Koscielny et al. [23] of a universal scaling law for daily maximum temperature anomalies. Estimated scaling exponents by DFA4 were 0.66 for maximum daily temperature ($T_{max}$), 0.57 for minimum daily temperature ($T_{min}$) and 0.66 for diurnal temperature range (DTR) in low elevation stations, 0.55 for $T_{max}$ and 0.54 for $T_{min}$ for mountain stations, 0.62 for $T_{max}$ and 0.71 for DTR in continental stations and 0.66, 0.68 respectively for maritime stations. They also found that correlations extend to almost three decades or more.

Fraedrich and Blender [9] estimated the spatial distribution of temperature scaling exponents from observations. They compared their results with those obtained from models under several assumptions for present and absent anthropogenic greenhouse effect. Their main conclusion was that temperature exhibits long memory with $h(2)$ about 0.65 for stations under maritime influence, while is does not for inner continent regions. The ocean effect on temperature scaling is more pronounced in mid-latitude maritime regions where almost $1/f$ noise is observed. In another framework Fraedrich et al. [10] propose an explanation on the physical mechanism resulting in the observed $1/f$ temperature spectrum over Atlantic and Pacific ocean midlatitude regions through a simple two-layer heat diffusion model.

Application of MF-DFA in river runoff and precipitation records [3, 4] suggests a 'non-universal' scaling behavior for both runoff and precipitation records. The multifractality for the runoff records is stronger and can be well described by a simple modified binomial multifractal model where only two parameters are needed:

$$h(q) = \frac{1}{q} - \frac{\ln(a^q + b^q)}{q \ln 2} \tag{2.8}$$

The agreement of the results with the fit suggests a 'universal' multifractal behavior for the runoff records [3, 4]. Precipitation records are in poor agreement with Eq. 2.8 and another approach is required for their description. Precipitation seems to have a more 'stochastic' behavior, so the assumption made for the runoff is that it is affected by water storage capacity of the basin and other climatic variables. Biswas et al. [24] used MF-DFA for the multifractal characterization of soil water storage. A long-term field experiment was conducted to obtain the data. Extreme (dry-wet) cases were selected for the soil water storage capacity. Analysis showed that multifractal scaling for water soil capacity varies as a result of the differences in micro climate in periods where storage increases. Heterogeneity is smoothened in the evapotranspiration periods where more uniform scaling is observed. In this case strong multifractality can be attributed to different scaling of large and small fluctuations. The need for more monitoring sites was emphasized for further scaling characterization of recharging periods.

# Chapter 3

# Data and Methods

## 3.1 Downward longwave radiation (DLR)

The Earth's radiation balance is determined by several factors ranging from the top atmosphere to the Earth's surface. The amount of energy reaching the top atmosphere includes a fraction that is reflected, while the remaining is the net incoming radiation. About 40% of the incoming radiation is infrared, 55% visible and 5% ultraviolet [25]. Once radiation enters the atmosphere it starts to interact with its components. The possible interactions are scattering and absorption. The above components are atmospheric molecules, aerosols and clouds. Absorbed radiation is re-emitted mainly as thermal (infrared, longwave, LW) radiation. 'Greenhouse' gases emit thermal while aerosols emit thermal and scatter shortwave [26] radiation. Earth's surface upwards radiation flux can be well approximated by a black body emission with an effective temperature $T_s$=290 K that takes into account the change of the black body surface temperature due to greenhouse warming [26]. Integrating Planck's function over all wavelengths, the flux density of black body (Stefan-Boltzmann law) is derived:

$$F = \sigma T^4 \tag{3.1}$$

where $\sigma$ is the Stefan-Boltzmann constant, equal to $5.67{\cdot}10^{-8}$ W/m$^2$/deg$^4$.

The estimation of the downwelling LW flux at the surface is less straightforward. The surface receives thermal radiation from all layers of the atmosphere above it, with each layer having a different temperature and different emissivity. Layers with larger temperatures and with larger emissivities emit more thermal radiation. The contribution of each layer to the surface radiation flux depends not only on its emissivity and temperature, but also on the transmissivity of the layers below it. Let us denote each atmospheric layer by the optical depth $\tau'$ between the top of the atmosphere and the layer. Layers with smaller $\tau'$ are situated higher than layers with larger $\tau'$. The maximum $\tau'$ is $\tau$, which is the optical depth of the whole atmospheric column. The Planck intensity of thermal radiation from a layer at the $\tau'$ layer is $B(\tau')$. With $\mu$ we describe the cosine of the zenith angle, which gives the direction of the radiation. $\mu$=1 means that the radiation travels straight down, while $\mu$=0 corresponds to horizontal beams. Then, the calculation of the downwelling LW radiation (DLR) at the surface can be performed by the double integral [25]:

$$F^{\downarrow}(\tau) = \int_{\tau'=0}^{\tau'=\tau} B(\tau') \left( \int_{\mu=0}^{\mu=1} e^{-(\tau-\tau')/\mu} \mathrm{d}\mu \right) \mathrm{d}\tau' \tag{3.2}$$

The DLR $F^{\downarrow}$ at the surface depends on the vertical profile of temperature in the atmosphere (through the Planck intensity $B$ of each layer) and on the vertical profile of humidity (through $\tau'$ at each layer). Large humidity at a layer, leads to larger $\tau'$ values and stronger emissivity and absorptivity.

The net longwave radiation flux on the surface is derived by the contribution of DLR from the atmo-

sphere and the surface emission. Conservation of energy results in the surface flux equation:

$$F^{\uparrow}_{net} = -F^{\downarrow} + \epsilon_s \sigma T_s^4 \tag{3.3}$$

where $\epsilon_s$ is a correction factor for Earth's radiative deviation from black body. This net radiative flux is the driver of all climatic processes at the surface and its accurate quantification is crucial in modeling and understanding surface phenomena. Therefore, also DLR $F^{\downarrow}$ is a main regulatory component of climate.

## 3.2 Organology

The Baseline Surface Radiation Network (BSRN) [27] records quality-controlled radiation fluxes at ground stations in diverse climatic regions, with a temporal resolution in the order of minutes. BSRN stations have to follow strict specifications for their instruments and methods. The measurement of DLR is performed with shaded and ventilated unmodified pyrgeometers. The target for the uncertainty level is 5% or 10 W/m$^2$ [28]. Pyrgeometers used are Eppley Precision Infrared Radiometer (PIR), with a transmission window approximately 3.5–50 $\mu$m, Eko MS-201 Precision Pyrgeometer permeable between 3–50 $\mu$m, Kipp and Zonen Delft CG4 Pyrgeometer with a spectral range 4.5–42 $\mu$m. The main parts of a pyrgeometer are a thermopile sensitive to a broad spectrum, a silicon dome permeable between $\sim$ 3–50 $\mu$m, a temperature sensor for measuring the body temperature of the instrument used for calibrations and corrections in the laboratory, and a sun shield to minimize the impact of instrument heating due to shortwave radiation.

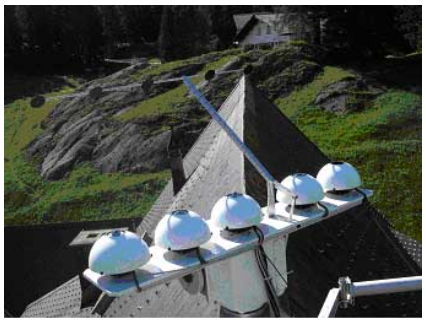

Figure 3.1: World infrared standard group of pyrgeometers (WISG) at PMOD/WRC

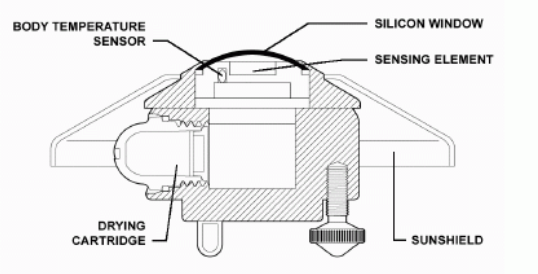


Figure 3.2: Main components of pyrgeometer

## 3.3 Measurements

Data were downloaded via ftp from the site of the Baseline Surface Radiation Network (BSRN) [28]. Among the many meteorological quantities available, the quantity of interest is DLR (W/m$^2$), available in one or three minutes resolution. The maximum time period covered is twenty years while stations with less than ten years coverage were rejected. Twenty-three stations were chosen. The spatial distribution of the selected stations spreads over almost all latitudes, but is highly focused in mid-latitude regions,

especially in the northern hemisphere. Over 50% of the stations are continental, either on mountain or low elevation. Coastal and maritime stations are also included and a variety of geophysical features are met.

| Station | Latitude ($^o$) | Longtitude ($^o$) | Altitude (m) | Period (years) | Incomplete(%) |
|---|---|---|---|---|---|
| asp | -23.80 | 133.80 | 547 | 18 | 12 |
| ber | 32.20 | -64.70 | 8 | 19 | 7 |
| bil | 36.60 | -98.00 | 317 | 19 | 10 |
| bon | 40.10 | -88.30 | 213 | 15 | 2 |
| bos | 40.10 | -105.20 | 1689 | 14 | 1 |
| bou | 40.10 | -105.00 | 1577 | 19 | 3 |
| clh | 36.90 | -75.10 | 37 | 13 | 8 |
| dra | 36.60 | -116.00 | 1007 | 12 | 2 |
| e13 | 36.60 | -97.50 | 318 | 19 | 12 |
| fpe | 48.30 | -105.10 | 634 | 15 | 4 |
| gcr | 34.30 | -89.87 | 98 | 15 | 4 |
| ilo | 8.50 | 4.60 | 350 | 13 | 63 |
| kwa | 8.70 | 167.70 | 10 | 18 | 4 |
| lau | -45.00 | 169.70 | 350 | 13 | 11 |
| man | -2.10 | 147.40 | 6 | 16 | 6 |
| nau | -0.50 | 166.90 | 7 | 14 | 5 |
| pay | 46.80 | 6.90 | 419 | 18 | 2 |
| psu | 40.70 | -78.00 | 376 | 12 | 2 |
| reg | 50.20 | -104.70 | 578 | 18 | 3 |
| spo | -89.90 | -24.80 | 2800 | 19 | 13 |
| syo | -69.00 | 39.60 | 18 | 18 | 3 |
| tam | 22.80 | 5.50 | 1385 | 13 | 1 |
| tat | 36.10 | 140.10 | 25 | 17 | 4 |

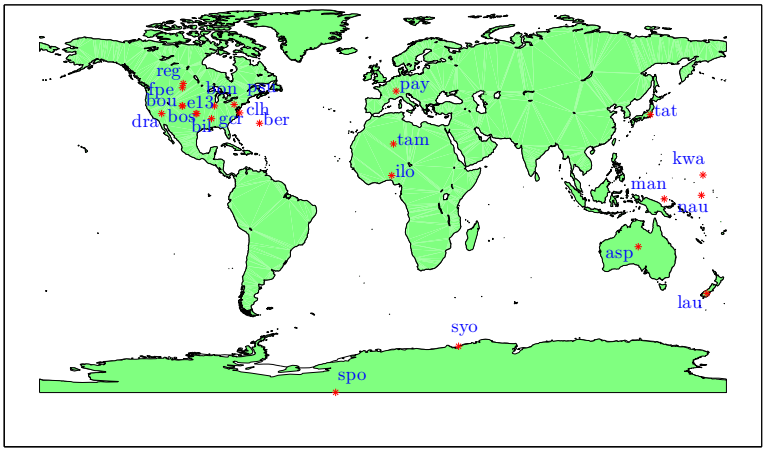


Figure 3.3: World map with the stations included in the analysis

## 3.4 Implementation of the method

We applied MF-DFA in the $q$ range of $-10 < q < 10$. We excluded the case of $q$=0 since another averaging procedure is needed and results of MF-DFA are questionable for this case [21]. When data were delivered in mixed resolutions we used as unit resolution the coarser found. This was done by segmenting all parts of timeseries with lower resolution to unit resolution segments and average each segment. In order to ensure that deseasonalization was sufficient, we divided by standard deviation of each unit resolution, of each hour, of each calendar day over all corresponding values during deseasonalization. The results were qualitatively unaffected, so we kept the first case to avoid homogenization of small and large fluctuations [4]. The detrending procedure was performed for up to third order polynomials. If no linear trends were observed we used the MF-DFA1, so possible crossovers at large scaling regions are not shifted to scales closer or larger than $N/4$ [15]. We shuffled the data in order to confirm that MF-DFA results are not due to a broad probability function and uncorrelated behavior was obtained.

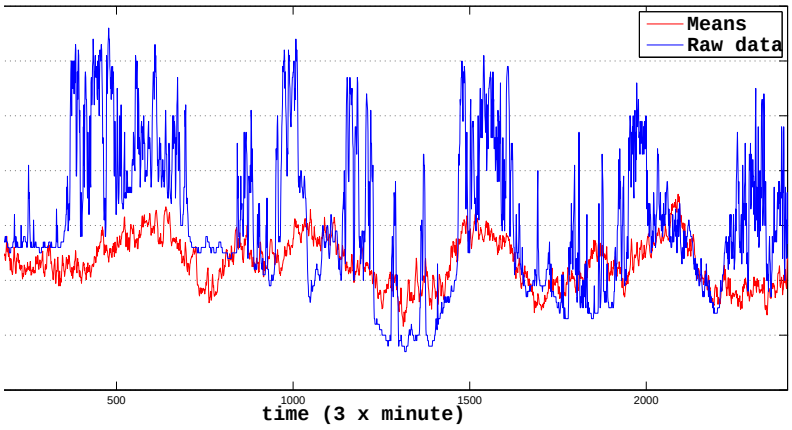


Figure 3.4: Comparison of raw data and mean values used for deseasonalization for five days period

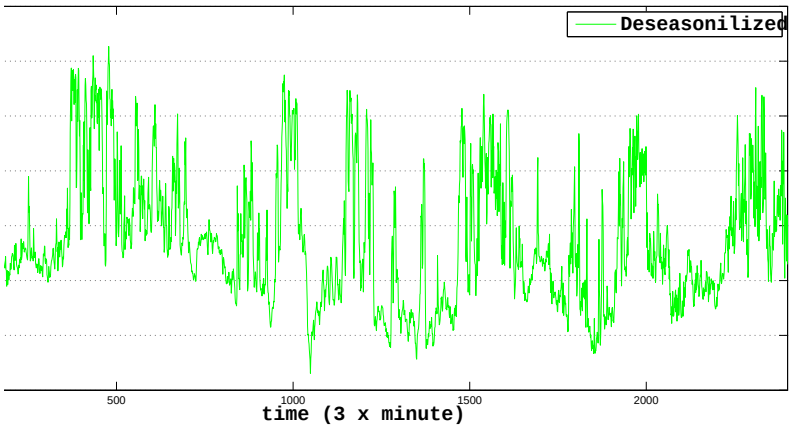


Figure 3.5: Deseasonalized data for five days period

## 3.5 Objectives of the study

In the present study correlation properties of DLR are examined by means of MF-DFA. Power law scaling of DLR second order fluctuations is investigated and possible general fluctuation function pattern

is searched. Varying scaling behavior in different scales can indicate the presence of physical processes affecting fluctuations. This can lead to the detection of locally set climate memory . Multi-fractal analysis is conducted in order to further resolve fluctuations behavior. Uncertainty over the observed features of the fluctuation function can be reduced and most robust results can be obtained. Moreover, undetected by second order fluctuations analysis, elements that affect fluctuations are possible to emerge through analyzing scaling exponents spectrum over all orders of fluctuations.

# Chapter 4

# Results

## 4.1 Crossovers

No significant difference was observed by using DFA(1-3). Fluctuations magnitude is reduced with increasing the order $l$ of the polynomial fit. This is an expected behavior since increasing the order of fit results in a fit with smaller residuals. The pattern of scaling remains unchanged for the different orders $l$, though. A typical fluctuation behavior starts with a large slope, corresponding to a non-stationary signal, up to time scale of about ten days. At this point a crossover occurs and for larger $s$ a smaller slope is observed, with values between 0.5 and 1, corresponding to positive correlations. A shift of the crossover to larger $s$ with increasing DFA order is noticed. The crossover existence could be attributed to AR correlations embedded in the signal, caused by meteorological processes with short-term memory. It this were true, the decay time of the AR process would be comparable to $s$ at the observed crossover.

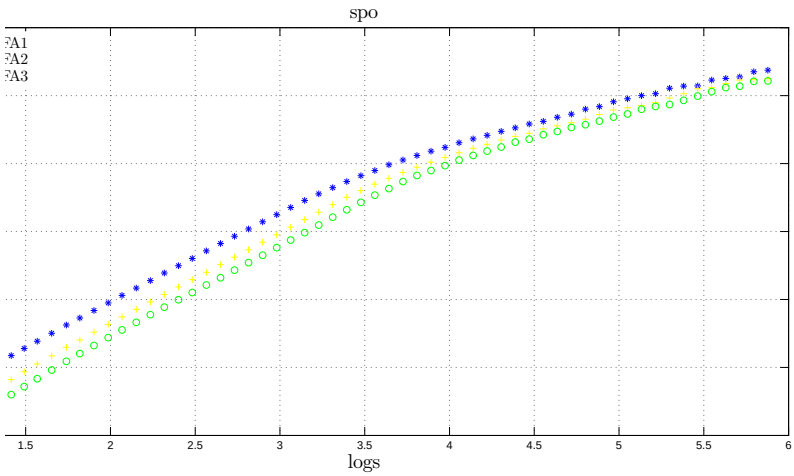


Figure 4.1: Comparison of different DFA orders for the South Pole station

An attempt to systematically detect the crossover was made. Based on the general pattern observed, we adopted a modified version of the empirical equation proposed by Cermak et al. [29] for trend-change point detection:

$$S = \frac{\min(p(t_l), p(t_r))}{|sl(t_l) - sl(t_r)| \cdot e(t_{l+r})} \tag{4.1}$$

where $S$ is the change point score. First, the data are fitted by a third order polynomial and at each point the trend to its left (subscript $l$) and its right (subscript $r$) is examined. $p$ is the probability of a trend being insignificant, $sl$ its slope, $e$ the trend fitting error, $t_l$, $t_r$, $t_{l+r}$ the trends to left, right and

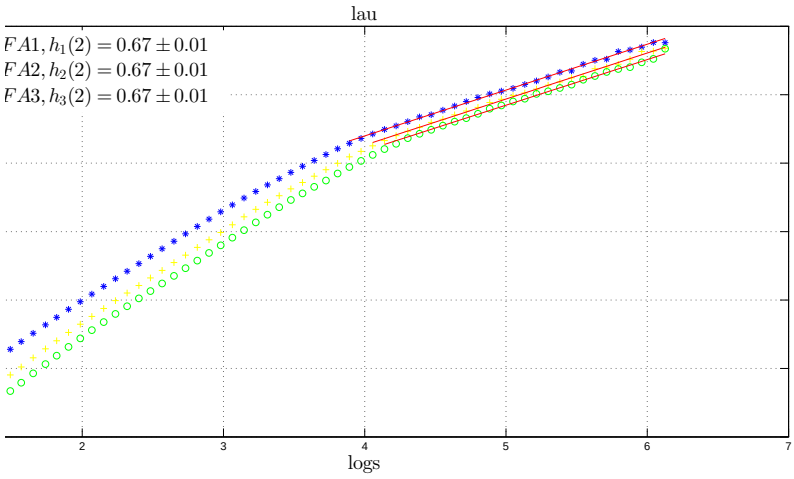


Figure 4.2: Comparison of different DFA orders for Lauder (New Zealand) station

combined subseries at the point being tested, respectively. The whole procedure is performed for a fixed width moving box, centered at the tested point. The point with the lowest score is the trend change point. Note that the intention is to minimize the numerator, while the denominator is maximized.

The main difference with our case is that we focus on a detection of the transition from a positive trend to another positive trend with smaller slope, which is not the case for Cermak et al. Therefore, we calculate for a fixed box size ($box$) the Euclidean distance between each consecutive point up to the center of the box($center$), sum the resulting values and normalize by the number of points used ($dist_{before}$):

$$dist_{before} = \frac{1}{(box-1)/2} \sum_{i=center-(box-1)/2}^{center} \sqrt{(log_{10}F_i - log_{10}F_{i-1})^2 + (log_{10}s_i - log_{10}s_{i-1})^2} \tag{4.2}$$

The same procedure is repeated starting from the box center to the end, $N$, of the series($dist_{after}$):

$$dist_{after} = \frac{1}{N-center} \sum_{i=center}^{N} \sqrt{(log_{10}F_i - log_{10}F_{i-1})^2 + (log_{10}s_i - log_{10}s_{i-1})^2} \tag{4.3}$$

Then we fit a line to the box values and estimate the fit standard error ($e$). Finally, for all points included in the box, the sum of consecutive points euclidean distances is calculated ($dist_{box}$):

$$dist_{box} = \sum_{i=center-(box-1)/2}^{center+(box-1)/2} \sqrt{(log_{10}F_i - log_{10}F_{i-1})^2 + (log_{10}s_i - log_{10}s_{i-1})^2} \tag{4.4}$$

The combination of the above statistics in a way that the numerator is minimized while the denominator is maximized for a moving box results in the empirical equation:

$$S = \frac{dist_{before} \cdot dist_{after}^7}{dist_{box} \cdot e} \tag{4.5}$$

which seems to successfully locate the crossover at the box center, when $S$ is minimized in a certain point win-

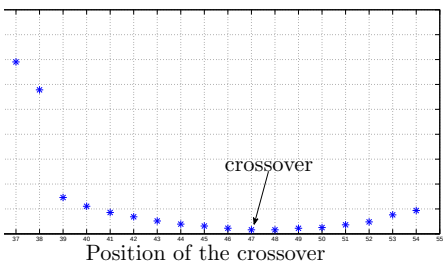


Figure 4.3: $S$ statistic for a window of 19 values of $F(s)$

dow, if the general pattern is nearly
followed. The above equation overweights the points after the box center. This is done in order to emphasize that a good linear fit at large $s$ is desirable, since the scaling factor $h$ is calculated from this region.

## 4.2 Periodic trends

Beyond the general scaling pattern described in the previous section, certain stations demonstrate differing scaling properties. The stations are Kwajalein, Nauru, and Bermuda and their scaling is presented in Figs. 4.4, 4.5, and 4.6, respectively. At least two crossovers are observed for each station, in different but comparable time scales between stations. Initially, the scaling narrowly follows $1/f$ noise. The first crossover occurs in scales comparable to those referred for the typical scaling pattern of the station majority, e.g. about ten days, but here it is less pronounced. A transitional scaling regime is located around the crossover followed by positively correlated scaling. The second crossover, also not very prominent, is observed at scales from about six months (for equatorial maritime stations in the western Pacific) to four years (for the mid-latitude station in the Bermudas). Flicker like $(1/f)$ noise follows, but for equatorial stations there is considerable scatter at these large $s$ and this creates difficulties in drawing any definite conclusion. However, this behavior is compatible with the presence of a strong signal with periodicity of a few years.

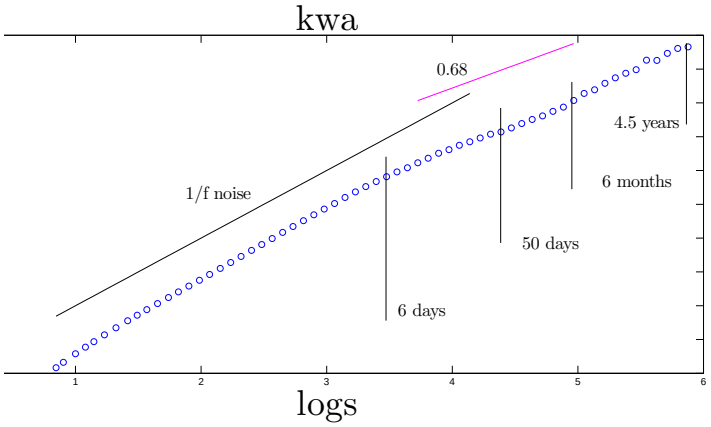


Figure 4.4: Fluctuation function for Kwajalein station

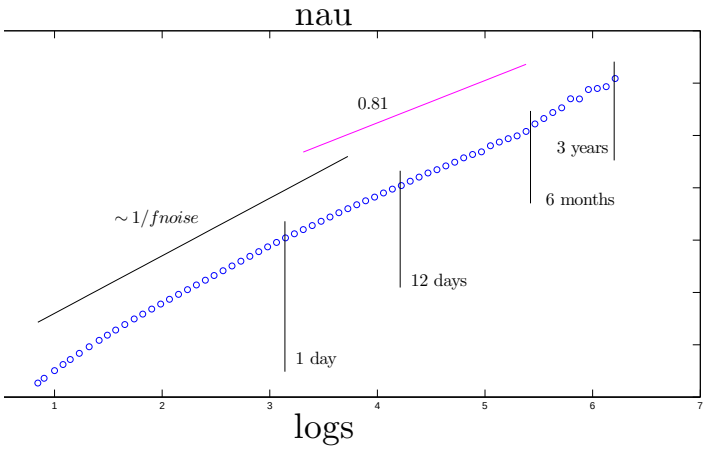


Figure 4.5: Fluctuation function for Nauru Island station

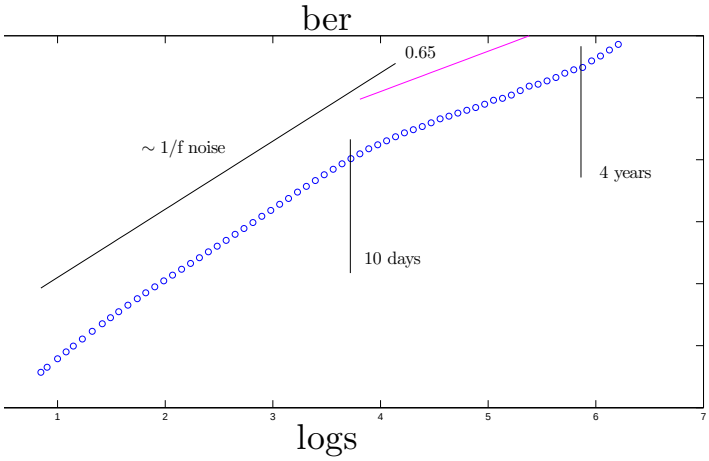


Figure 4.6: Fluctuation function for Bermudas station

In an attempt to decompose the obtained signal for the equatorial stations we considered the influence of the El Niño Southern Oscillation (ENSO). The ENSO is a quasiperiodic climate pattern with a period of about five years, affecting the tropical western Pacific area. We examine the effect of a sinusoidal ENSO signal on DLR with a locally determined amplitude. Determining the amplitude is difficult due to the ENSO spatial variability, but a reasonable estimation is $\sim$10 W/m$^2$, according to Pavlakis et al. [30] for the Nino-3.4 region and bordering areas. We used the superposition rule, Eq. 2.7, for correlated noise $F_n$ and sinusoidal trend $F_t$, with five years period $T$ and adjusted amplitude $A$. $F_n$ was estimated as:

$$F_n(s) = b_1 \cdot s^h \tag{4.6}$$

where $b_1$ is an adjustable parameter for the magnitude of the noise and $h$ is the scaling exponent.

$F_t$ was approximated by a linear trend up to the scale of the sine period [15] and afterwards was considered constant:

$$F_t(s) = b_2 \cdot \frac{A}{T} \cdot s^a, s \leq T \tag{4.7}$$

$$F_t(s) = \frac{1}{2\sqrt{2}\pi} A \cdot T, s > T \tag{4.8}$$

where $b_2$ is an adjustable parameter for the magnitude of trends fluctuations and $a$ is the trend's slope.

The superposition rule does not quite reproduce the observed scaling behavior at scales where $F_{nt}$ is determined by $F_t$. This is more pronounced for Kwajalein station (Fig. 4.7), while for Nauru Island station (Fig. 4.8) a better fit is obtained. Different tuning for Kwajalein produces slightly better agreement, but $A$ has to be very small, down to just 2 W/m$^2$.

However, some qualitative properties seem to be well detected. For example, the point where $F_{nt}$ starts to deviate from $F_n$ is in agreement with observed $F$ values. Possible reasons for the discrepancy are imperfect deseasonalization, poor model tuning, and the finite size of the timeseries. Seasonality can never be completely removed, especially if strong interannual oscillation is involved. Fig. 4.9 for Momote station indicates where $F_{nt}$ is considerably larger than the sine amplitude, that a remaining annual cycle can disturb fluctuations at the 'asymptotic' region. Also, due to the limitation of the records length, the last values of $F$ can be somewhat scattered. Finally model assumption was that $F_t$ scales according to equations 4.7, 4.8. This does not hold for small regimes, spread around the crossovers, where a quadratic behavior is expected [15].

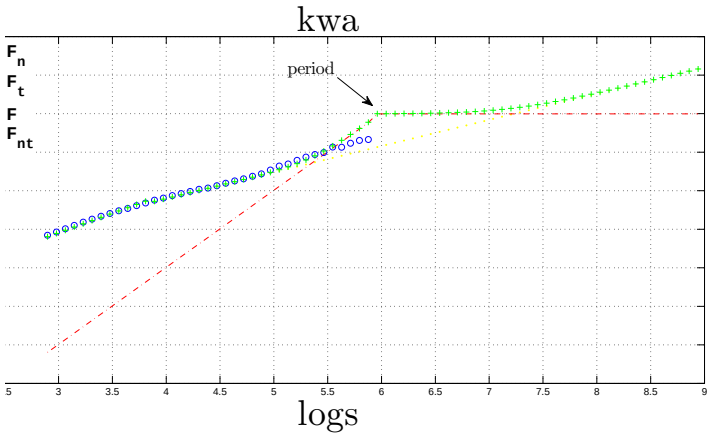


Figure 4.7: Observed, superpositioned and component fluctuations functions for Kwajalein station. $A$ is assumed 8 W/m$^2$

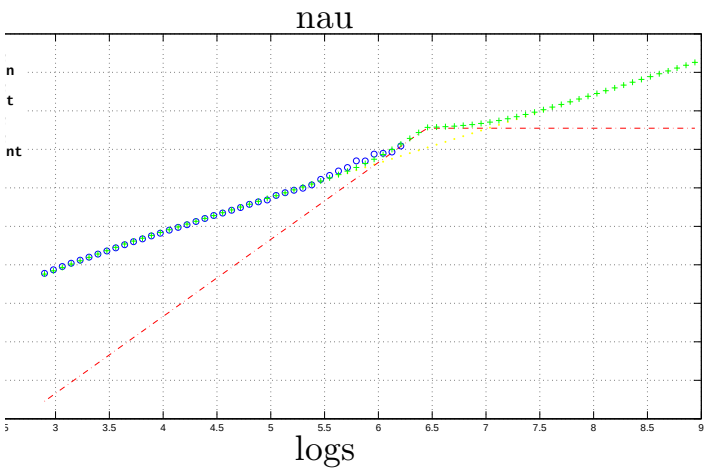


Figure 4.8: Observed, superpositioned and component fluctuations functions for Nauru Island station. $A$ is assumed 12 W/m$^2$

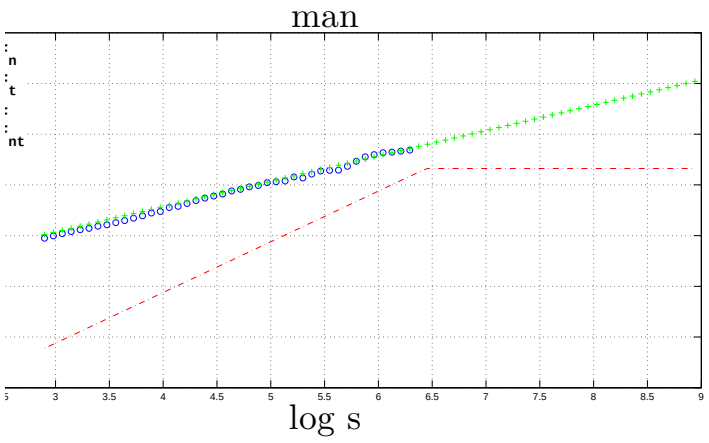


Figure 4.9: Observed, superpositioned and component fluctuations functions for Momote station. $A$ is assumed 15 W/m$^2$

## 4.3 Long memory

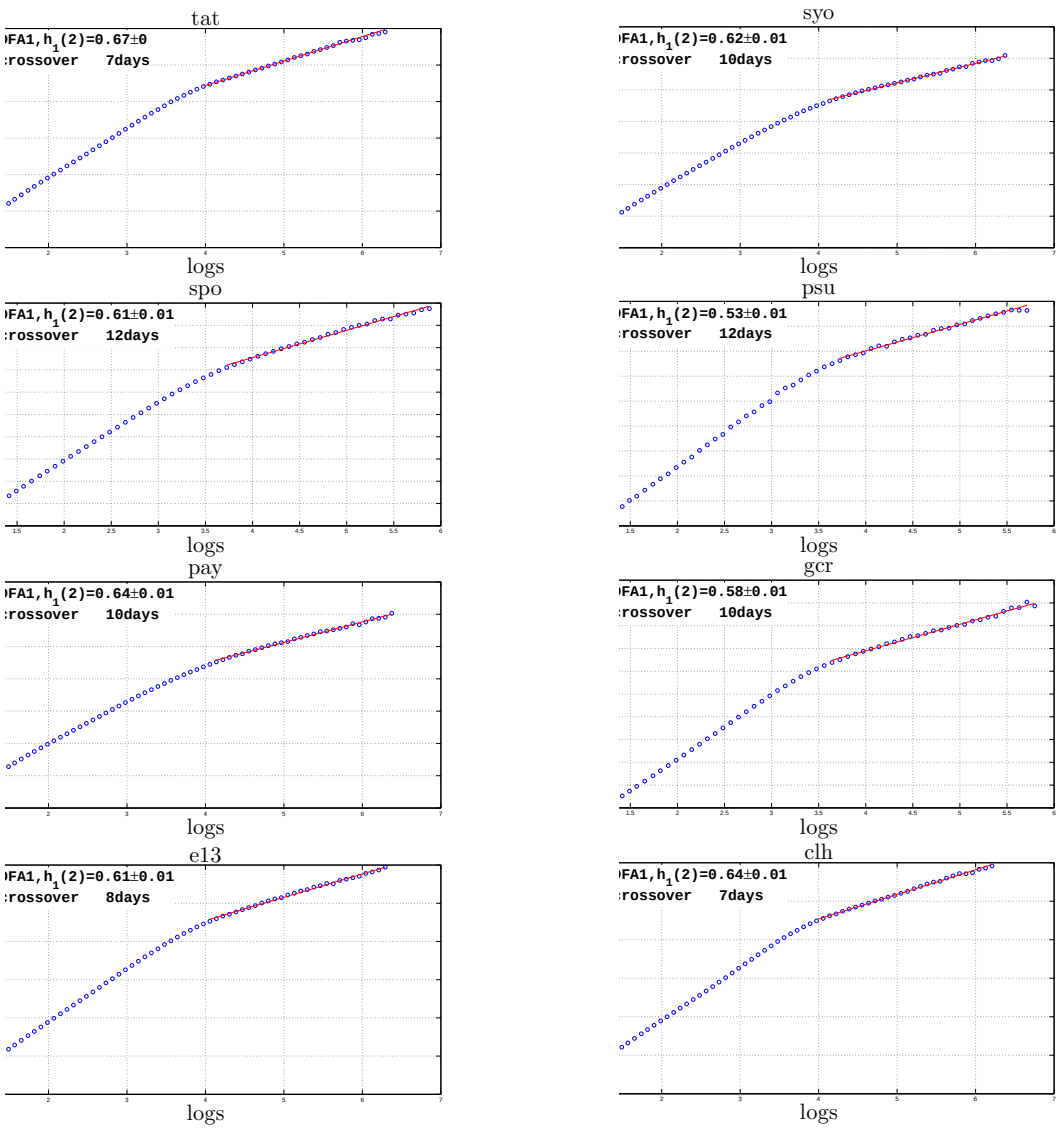


Figure 4.10: Crossovers and estimated scaling exponents $h(2)$

In Section 4.1 the crossover position was determined in order to provide a good estimation of the scaling exponent $h(2)$ for large time scales $s$. So called long climate 'memory' for DLR is expected to be consistent with air surface temperature findings [22, 9, 10, 31, 2], since temperature is highly correlated with DLR according to Eqs. 3.1, 3.2, and 3.3.

In Fig. 4.10, observed memory is shown for stations following the general pattern described in Section 4.1. Note that station Ilorin was excluded from the analysis since 66% of the measurements were missing and spurious results could be obtained [16]. Overall memory for stations where no imposed periodic trends are inspected is shown in Fig. 4.11. Mean value of scaling exponent in asymptotic regions is 0.63. This is in good agreement with mean memory estimation ($\approx 0.65$) for temperature by models and observations.

Due to the limited number of stations and their uneven geographical distribution a reliable latitude and/or altitude dependence of memory cannot be examined. This is clear in figures 4.12, 4.13 where the stations sample is unequally distributed and possible h(2) altitude-latitude correlation cannot be investigated.

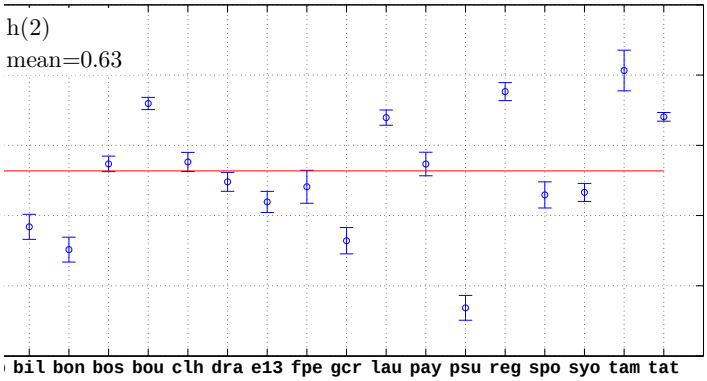


Figure 4.11: Estimated $h(2)$ exponents, except for stations with periodic trend inspection

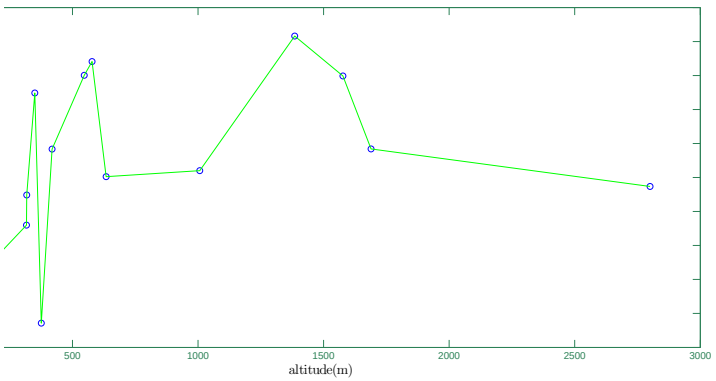


Figure 4.12: Estimated $h(2)$ exponents versus altitude

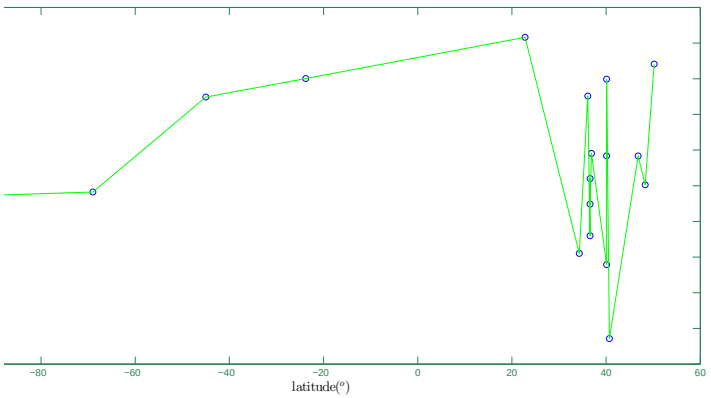


Figure 4.13: Estimated $h(2)$ exponents versus latitude

## 4.4 Multifractal characterization

Examining the whole spectrum of moments of the fluctuation function $F_q(s)$ can provide better understanding of the results obtained in Sections 4.2, 4.3. Also the characterization of data as monofractal or multifractal can provide information on different scaling properties of small and large fluctuations.

Scaling exponents are calculated for $s$ >25 days. This threshold is used since scaling of $F_2(s)$ is established in such scales for stations following the observed scaling pattern.

In Fig 4.14, 4.15, 4.16, 4.17 the $h(q)$ dependence on $q$ is shown. $h(q)$ values are increasing monotonically with decreasing $q$. This is an expected behavior for multifractal data. However, error bounds do not follow the prospective [17] course. For positive $q$ values, the error bounds are expected to be small and relatively consistent, while for negative $q$ should be much larger. Also, the observed increase of $h(q)$ with decreasing $q$, though present, seems to deviate from the theoretical [17] pattern for Gaussian data. This can be due to short range correlations, which induce a crossover discussed in Section 4.1, and disturb multifractality in a way that is shown in Fig 2.2.

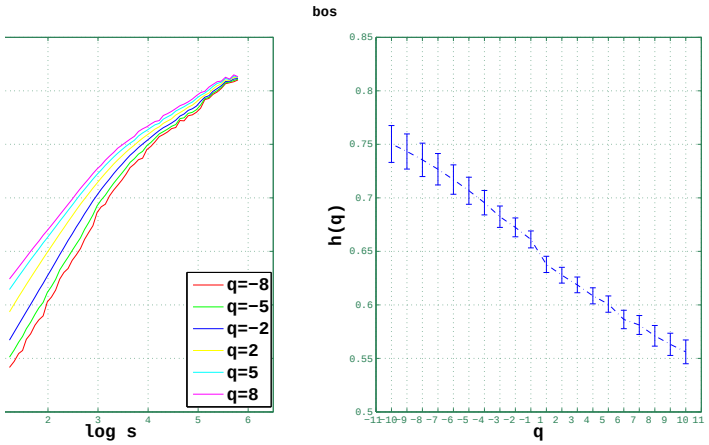


Figure 4.14: Fluctuations functions and scaling exponents spectrum of Bondville station

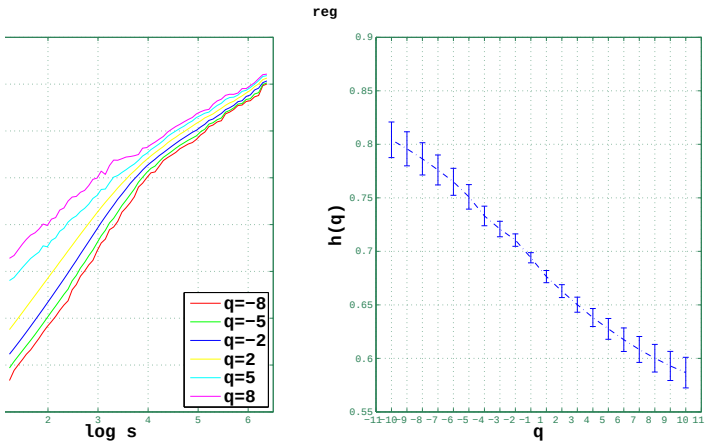


Figure 4.15: Fluctuations functions and scaling exponents spectrum of Regina station

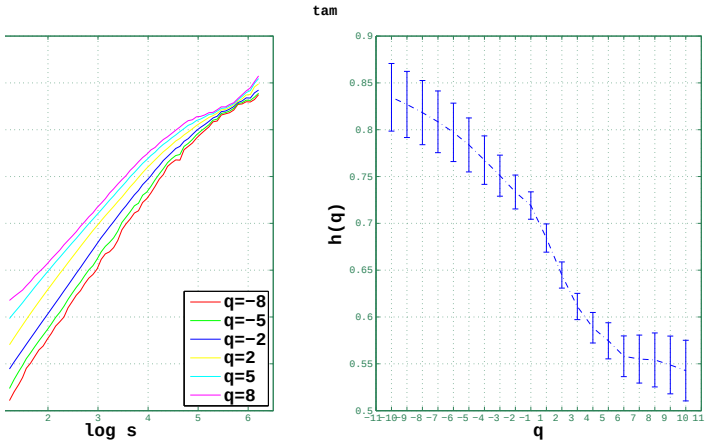


Figure 4.16: Fluctuations functions and scaling exponents spectrum of Tamanrasset station

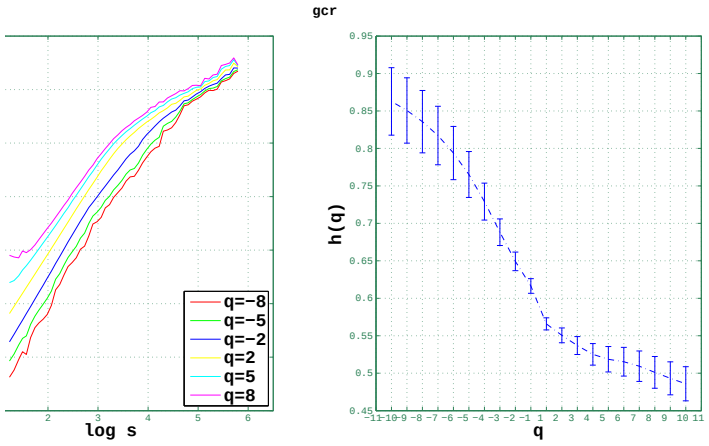


Figure 4.17: Fluctuations functions and scaling exponents spectrum of Goodwin Creek station

The existence of periodic trends in certain stations, examined in section 4.2, is confirmed by looking all moments of $F_q(s)$. In Fig 4.18, 4.19, 4.20, 4.21 multifractality is corrupted in a certain way. A peak of h(q) appears, or tends to appear, for q around zero. This is consistent with Ludescher et al. [17] findings on how periodicities affect multifractal scaling. Different extent of multifractality corruption can be explained by varying amplitude and period of the trend, as well as by combined corruption from short range correlations.

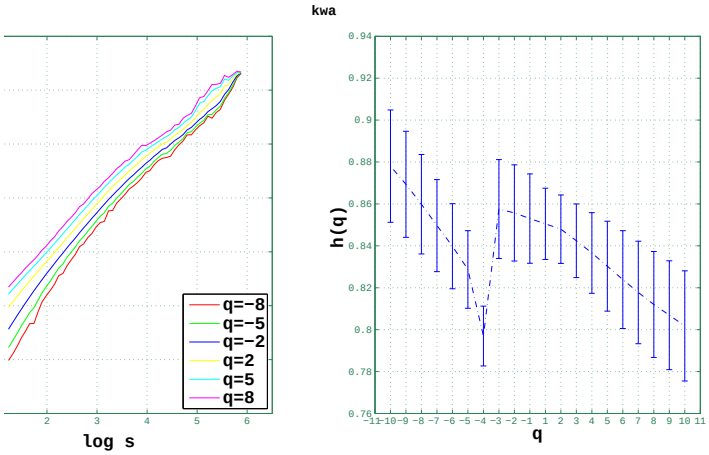


Figure 4.18: Multifractal spectrum of Kwajalein station

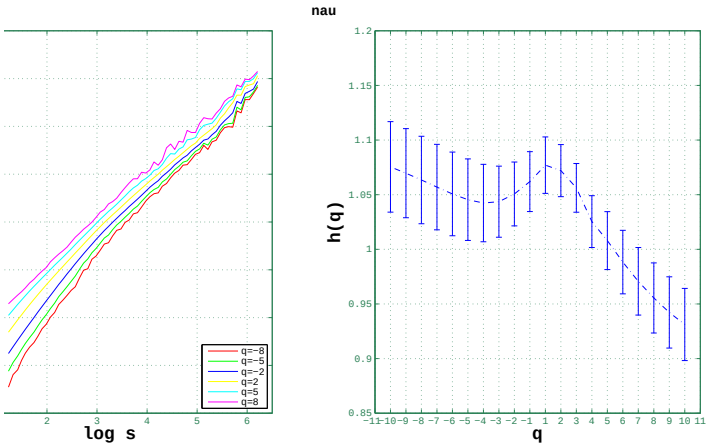


Figure 4.19: Multifractal spectrum of Nauru Island station

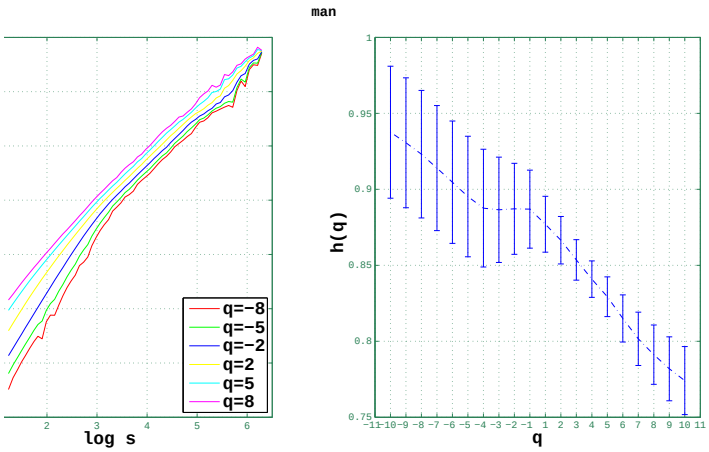


Figure 4.20: Multifractal spectrum of Momote station

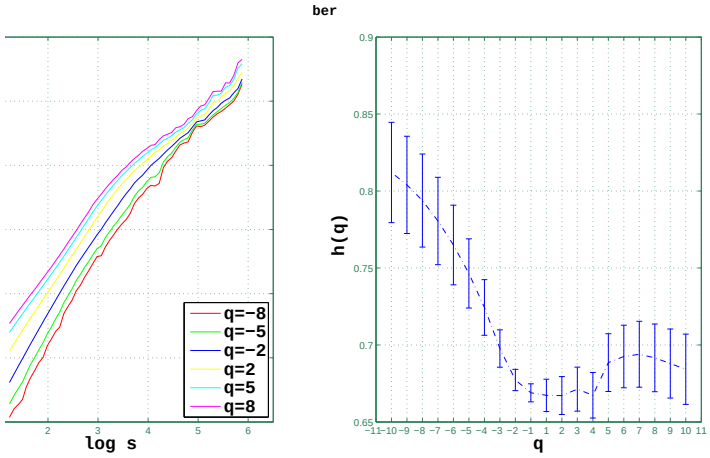


Figure 4.21: Multifractal spectrum of Bermuda station

Corrupted multifractality is also observed in other stations. In Fig. 4.22 the $h(q)$ spectrum for Lauder station, situated at new Zealand, suggests the presence of an oscillatory trend, mainly affecting small fluctuations (e.g. negative $q$ values). This can be attributed to a weakened ENSO effect at the region affecting small fluctuations.

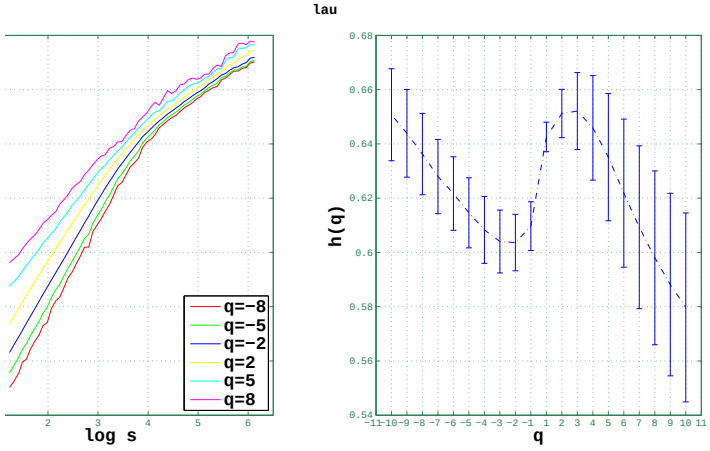


Figure 4.22: Multifractal spectrum of Lauder station

# Chapter 5

# Conclusions

Summarizing the results of the previous chapter we conclude that fluctuation function $F_2(s)$ of DLR scales like a power law with a typical pattern. This pattern involves $1/f$ noise up to a scale of about ten days, where a crossover occurs, followed by positive correlations. A systematic attempt to locate the crossover resulted in the empirical formula given by Eq. 4.5.

In cases where the general pattern was not observed, oscillatory trends seem to influence the fluctuation function $F_q(s)$. In micro-scales 1/f noise is observed. For the case of the equatorial , under maritime influence, stations in western Pacific the possible impact in $F_q(s)$ by ENSO was examined. The attempt to decompose the observed signal of $F_2(s)$ as a superposition of noise and oscillatory fluctuations did not quite reproduce the original signal. However some qualitative features regarding the starting point where superposed signal is dominated by oscillatory fluctuations are common in both synthetic and observed signal. This of course holds only for stations where the relative magnitudes of $F_2(s)_n$ and $F_2(s)_t$ are comparable in a certain s region. In addition, concerning the western Pacific equatorial stations, examining the spectrum of scaling exponents derived from all moments of fluctuations $F_q(s)$ indicates similar multifractality corruption due to periodic trends. This was observed in all stations at the broader west Pacific region, regardless of whether it was apparent during second moment fluctuations($F_2(s)$) analysis. The combination of above findings strongly indicates that ENSO has a prominent effect in the fluctuations of DLR at the west Pacific area.

The estimated mean memory for stations where no periodicities are present is 0.63. This is consistent with the estimated mean memory of temperature, confirming the theoretically expected correlation between the two quantities. The spatial distribution of scaling exponents could not be examined due to limitations from geographic distribution and number of stations. Examining more representative stations is necessary for the extraction of possible correlations results among DLR scaling and altitude, latitude and maritime influence.

Multifractal analysis for stations whose $F_2(s)$ fluctuations follow the 'general' pattern, without any apparent periodicities, revealed that DLR presents multifractal scaling that seems to approximate the expected pattern for Gaussian multifractal data. Deviations from the theoretical pattern could be attributed to short-range correlations embedded in the data.

# Bibliography


[1] P Talkner and RO Weber. Power spectrum and detrended fluctuation analysis: Application to daily temperatures. *PHYSICAL REVIEW E*, 62(1, Part a):150–160, JUL 2000.

[2] M. N. Efstathiou, C. Tzanis, A. P. Cracknell, and C. A. Varotsos. New features of land and sea surface temperature anomalies. *INTERNATIONAL JOURNAL OF REMOTE SENSING*, 32(11, SI):3231–3238, 2011.

[3] JW Kantelhardt, D Rybski, SA Zschiegner, P Braun, E Koscielny-Bunde, V Livina, S Havlin, and A Bunde. Multifractality of river runoff and precipitation: comparison of fluctuation analysis and wavelet methods. *PHYSICA A-STATISTICAL MECHANICS AND ITS APPLICATIONS*, 330(1-2):240–245, DEC 1 2003. International Workshop in honor of Shlomo Havlins 60th Birthday, ELAT, ISRAEL, JAN 05-09, 2003.

[4] JW Kantelhardt, E Koscielny-Bunde, D Rybski, P Braun, A Bunde, and S Havlin. Long-term persistence and multifractality of precipitation and river runoff records. *JOURNAL OF GEOPHYSICAL RESEARCH-ATMOSPHERES*, 111(D1), JAN 14 2006.

[5] C Matsoukas, S Islam, and I Rodriguez-Iturbe. Detrended fluctuation analysis of rainfall and streamflow time series. *JOURNAL OF GEOPHYSICAL RESEARCH-ATMOSPHERES*, 105(D23):29165–29172, DEC 16 2000.

[6] RB Govindan, D Vyushin, A Bunde, S Brenner, S Havlin, and HJ Schellnhuber. Global climate models violate scaling of the observed atmospheric variability. *PHYSICAL REVIEW LETTERS*, 89(2), JUL 8 2002.

[7] Xiuhua Zhu, Klaus Fraedrich, Zhengyu Liu, and Richard Blender. A Demonstration of Long-Term Memory and Climate Predictability. *JOURNAL OF CLIMATE*, 23(18):5021–5029, SEP 2010.

[8] Diego Rybski, Armin Bunde, and Hans von Storch. Long-term memory in 1000-year simulated temperature records. *JOURNAL OF GEOPHYSICAL RESEARCH-ATMOSPHERES*, 113(D2), JAN 19 2008.

[9] K Fraedrich and R Blender. Scaling of atmosphere and ocean temperature correlations in observations and climate models. *PHYSICAL REVIEW LETTERS*, 90(10), MAR 14 2003.

[10] K Fraedrich, U Luksch, and R Blender. 1/f model for long-time memory of the ocean surface temperature. *PHYSICAL REVIEW E*, 70(3, Part 2), SEP 2004.

[11] R Blender, K Fraedrich, and B Hunt. Millennial climate variability: GCM-simulation and Greenland ice cores. *GEOPHYSICAL RESEARCH LETTERS*, 33(4), FEB 25 2006.

[12] JW Kantelhardt, SA Zschiegner, E Koscielny-Bunde, S Havlin, A Bunde, and HE Stanley. Multifractal detrended fluctuation analysis of nonstationary time series. *PHYSICA A-STATISTICAL MECHANICS AND ITS APPLICATIONS*, 316(1-4):87–114, DEC 15 2002.

[13] Peng et al. Mosaic organization of DNA nucleotides. *PHYSICAL REVIEW E*, 49(2):1685–1689, FEB 1994.

[14] JW Kantelhardt, E Koscielny-Bunde, HHA Rego, S Havlin, and A Bunde. Detecting long-range correlations with detrended fluctuation analysis. *PHYSICA A*, 295(3-4):441–454, JUN 15 2001.

[15] Z Chen, K Hu, P Carpena, P Bernaola-Galvan, HE Stanley, and PC Ivanov. Effect of trends on detrended fluctuation analysis. *PHYSICAL REVIEW E*, 64, JUN 26 2001.

[16] Z Chen, PC Ivanov, K Hu, and HE Stanley. Effect of nonstationarities on detrended fluctuation analysis. *PHYSICAL REVIEW E*, 65(4, Part 1), APR 2002.

[17] Josef Ludescher, Mikhail I. Bogachev, Jan W. Kantelhardt, Aicko Y. Schumann, and Armin Bunde. On spurious and corrupted multifractality: The effects of additive noise, short-term memory and periodic trends. *PHYSICA A-STATISTICAL MECHANICS AND ITS APPLICATIONS*, 390(13):2480–2490, JUL 1 2011.

[18] D Maraun, HW Rust, and J Timmer. Tempting long-memory - on the interpretation of DFA results. *NONLINEAR PROCESSES IN GEOPHYSICS*, 11(4):495–503, 2004.

[19] Tiziana Simoniello, Rosa Coppola, Vincenzo Cuomo, Mariagrazia D'Emilio, Maria Lanfredi, Margherita Liberti, and Maria Macchiato. SEARCHING FOR PERSISTENCE IN ATMOSPHERIC TEMPERATURE TIME SERIES: A RE-VISITATION OF RESULTS FROM DETRENDED FLUCTUATION ANALYSIS. *INTERNATIONAL JOURNAL OF MODERN PHYSICS B*, 23(28-29):5417–5423, NOV 20 2009. Workshop on Modelling Geophysical Systems by Statistical Mechanics Methods, Erice, ITALY, APR 27-MAY 02, 2008.

[20] M. Lanfredi, T. Simoniello, V. Cuomo, and M. Macchiato. Discriminating low frequency components from long range persistent fluctuations in daily atmospheric temperature variability. *ATMOSPHERIC CHEMISTRY AND PHYSICS*, 9(14):4537–4544, 2009.

[21] S. Lovejoy and D. Schertzer. Haar wavelets, fluctuations and structure functions:convenient choices for geophysics. *NONLINEAR PROCESSES IN GEOPHYSICS*, 513(19):513–527, SEP 13 2012.

[22] RO Weber and P Talkner. Spectra and correlations of climate data from days to decades. *JOURNAL OF GEOPHYSICAL RESEARCH-ATMOSPHERES*, 106(D17):20131–20144, SEP 16 2001.

[23] Eva Koscielny-Bunde, Armin Bunde, Shlomo Havlin, H. Eduardo Roman, Yair Goldreich, and Hans-Joachim Schellnhuber. Indication of a Universal Persistence Law Governing Atmospheric Variability. *PHYSICAL REVIEW LETTERS*, 81(3), JUL 20 1998.

[24] A. Biswas, T. B. Zeleke, and B. C. Si. Multifractal detrended fluctuation analysis in examining scaling properties of the spatial patterns of soil water storage. *NONLINEAR PROCESSES IN GEOPHYSICS*, 19(2):227–238, 2012.

[25] FW Taylor IM Vardavas. *Radiation and Climate*. OXFORD UNIVERSITY PRESS, 2007.

[26] KN LIOU. *An Introduction to Atmospheric Radiation*. ACADEMIC PRESS, 2002.

[27] Ohmura A., E. Dutton, B. Forgan, C. Frohlich, H. Gilgen, H. Hegne, A. Heimo, G. Koenig-Langlo, B. McArthur, G. Muller, R. Philipona, C. Whitlock, K. Dehne, and M. Wild. Baseline Surface Radiation Network (BSRN/WCRP): New precision radiometry for climate change research. *BULLETIN OF THE AMERICAN METEOROLOGICAL SOCIETY*, 79(10):2115–2136, 1998.

[28] http://www.bsrn.awi.de/en/home/.

[29] Jan Cermak, Martin Wild, Reto Knutti, Michael I. Mishchenko, and Andrew K. Heidinger. Consistency of global satellite-derived aerosol and cloud data sets with recent brightening observations. *GEOPHYSICAL RESEARCH LETTERS*, 37, NOV 5 2010.

[30] K. G. Pavlakis, D. Hatzidimitriou, E. Drakakis, C. Matsoukas, A. Fotiadi, N. Hatzianastassiou, and I. Vardavas. ENSO surface longwave radiation forcing over the tropical Pacific. *ATMOSPHERIC CHEMISTRY AND PHYSICS*, 7(8):2013–2026, 2007.

[31] Klaus Fraedrich, Richard Blender, and Xiuhua Zhu. CONTINUUM CLIMATE VARIABILITY: LONG-TERM MEMORY, SCALING, AND 1/F-NOISE. *INTERNATIONAL JOURNAL OF MODERN PHYSICS B*, 23(28-29):5403–5416, NOV 20 2009. Workshop on Modelling Geophysical Systems by Statistical Mechanics Methods, Erice, ITALY, APR 27-MAY 02, 2008.